

Fundamental stellar parameters of benchmark stars from CHARA interferometry

III. Giant and subgiant stars[★]

I. Karovicova¹, T. R. White^{2,3}, T. Nordlander^{4,5}, L. Casagrande^{4,5}, M. Ireland⁴, and D. Huber⁶

¹ Landessternwarte, University of Heidelberg, Königstuhl 12, 69117 Heidelberg, Germany
e-mail: karovicova@uni-heidelberg.de

² Sydney Institute for Astronomy (SfA), School of Physics, University of Sydney, NSW 2006, Australia

³ Stellar Astrophysics Centre (SAC), Department of Physics and Astronomy, Aarhus University, Ny Munkegade 120, 8000 Aarhus C, Denmark

⁴ Research School of Astronomy and Astrophysics, Australian National University, Canberra ACT 2611, Australia

⁵ Center of Excellence for Astrophysics in Three Dimensions (ASTRO-3D), Stromlo, Australia

⁶ Institute for Astronomy, University of Hawai'i, 2680 Woodlawn Drive, Honolulu, HI 96822, USA

Received 24 August 2021 / Accepted 27 September 2021

ABSTRACT

Context. Large spectroscopic surveys of the Milky Way must be calibrated against a sample of benchmark stars to ensure the reliable determination of atmospheric parameters.

Aims. Here, we present new fundamental stellar parameters of seven giant and subgiant stars that will serve as benchmark stars for large surveys. The aim is to reach a precision of 1% in the effective temperature. This precision is essential for accurate determinations of the full set of fundamental parameters and abundances for stars observed by the stellar surveys.

Methods. We observed HD 121370 (η Boo), HD 161797 (μ Her), HD 175955, HD 182736, HD 185351, HD 188512 (β Aql), and HD 189349, using the high angular resolution optical interferometric instrument PAVO at the CHARA Array. The limb-darkening corrections were determined from 3D model atmospheres based on the STAGGER grid. The T_{eff} were determined directly from the Stefan-Boltzmann relation, with an iterative procedure to interpolate over tables of bolometric corrections. We estimated surface gravities from comparisons to Dartmouth stellar evolution model tracks. The spectroscopic observations were collected from the ELODIE and FIES spectrographs. We estimated metallicities ([Fe/H]) from a 1D non-local thermodynamic equilibrium (NLTE) abundance analysis of unblended lines of neutral and singly ionised iron.

Results. For six of the seven stars, we measured the value of T_{eff} to better than 1% accuracy. For one star, HD 189349, the uncertainty on T_{eff} is 2%, due to an uncertain bolometric flux. We do not recommend this star as a benchmark until this measurement can be improved. Median uncertainties for all stars in $\log g$ and [Fe/H] are 0.034 dex and 0.07 dex, respectively.

Conclusions. This study presents updated fundamental stellar parameters of seven giant and subgiant stars that can be used as a new set of benchmarks. All the fundamental stellar parameters were established on the basis of consistent combinations of interferometric observations, 3D limb-darkening modelling, and spectroscopic analysis. This paper in this series follows our previous papers featuring dwarf stars and stars in the metal-poor range.

Key words. standards – techniques: interferometric – surveys

1. Introduction

Large stellar surveys are collecting a vast amount of data that allows us to investigate the properties of stars and planets and, thus, to explore our Galaxy in greater detail. These surveys include *Gaia* (Gaia Collaboration 2016), APOGEE (Allende Prieto et al. 2008), GALAH (De Silva et al. 2015), *Gaia*-ESO (Gilmore et al. 2012; Randich & Gilmore 2013), and the future 4MOST survey (de Jong et al. 2012). The quality of the information that can be extracted from the data observed by these surveys is strongly affected by the ability to properly test and correctly scale the stellar models applied to the surveys. This objective is achieved with assistance of a sample of stars with

highly reliable fundamental stellar parameters, known as benchmark stars.

It is crucial to determine the fundamental stellar parameters of benchmark stars with the highest possible precision. These parameters include the effective temperature (T_{eff}), surface gravity ($\log g$), metallicities ([Fe/H]), and radius. This is particularly important with regard to the effective temperature. This parameter is traditionally determined by using stellar spectroscopy. This technique unfortunately allows for only an indirect determination of T_{eff} , leading to model dependencies that can negatively affect the accuracy of delivered results. Lebzelter et al. (2012) points out the difficulties, especially when modelling giants, due to increased non-LTE effects and to the differences between models.

For some stars, however, it is possible to directly determine T_{eff} with only minor model dependencies. Optical interferometry

[★] Tables A.1–A.7 are only available at the CDS via anonymous ftp to cdsarc.u-strasbg.fr (130.79.128.5) or via <http://cdsarc.u-strasbg.fr/viz-bin/cat/J/A+A/658/A48>

offers this ideal approach by allowing for the precise measurement of the angular diameter, θ (e.g., Boyajian et al. 2012a,b, 2013; von Braun et al. 2014; Ligi et al. 2016; Baines et al. 2018; Rabus et al. 2019; Rains et al. 2020). From the angular diameter, in combination with the bolometric flux, F_{bol} , the effective temperature, T_{eff} , can be determined directly as described by the Stefan-Boltzmann relation. We note the effective temperatures determined in this manner are only weakly model-dependent via adopted bolometric and limb-darkening corrections. Stars with interferometrically derived T_{eff} are, therefore, ideal benchmarks for calibrating spectroscopic surveys.

Currently, there is only a limited sample of interferometrically observed benchmark stars that has been defined. These are 34 stars selected for the *Gaia*-ESO survey (Jofré et al. 2014; Heiter et al. 2015). However, even though the angular diameters of the *Gaia*-ESO benchmark stars were observed using optical interferometry and, therefore, the T_{eff} were directly determined, the measurements were selected from the literature, applying inconsistent limb-darkening corrections from various model atmosphere grids, leading to strong inconsistencies within the sample. This set is limited to a coarse sample of the stellar parameter space and, moreover, it is biased in terms of the stellar age (Sahlholdt et al. 2019).

We have established a program to expand the sample of benchmark stars. In general, we aim to both expand the sample and deliver highly reliable fundamental stellar parameters of stars covering a wide range of parameter space. Our sample includes stars that expand the parameter space of the current benchmark sample, as well as stars listed as *Gaia*-ESO benchmarks, for which we seek to confirm and revise their parameters, as well as stars that have been proposed as potential benchmarks by Heiter et al. (2015).

As a first step within this programme, we observed three important *Gaia*-ESO metal-poor benchmark stars (Karovicova et al. 2018). We resolved previously reported differences between T_{eff} derived by spectroscopy, photometry, and interferometry pointed out by Heiter et al. (2015). We further expanded the sample to include a set of ten metal-poor benchmark stars (Karovicova et al. 2020). Most recently, we determined the properties of nine dwarf stars (Karovicova et al. 2021). Overall, the published samples include updated stellar parameters for four *Gaia*-ESO benchmarks and for 15 entirely new benchmarks. This comprises the subject of the next paper in this series, which is based on the investigation of seven giant and subgiant stars, including one of the *Gaia*-ESO benchmarks. The recommended stars will serve as standards for validating current and future large stellar surveys, as well as to help in calibrating the characterization of exoplanet host stars (Tayar et al. 2020).

2. Observations

2.1. Science targets

The third set of targets from our sample are seven giant and subgiant stars HD 121370 (η Boo), HD 161797 (μ Her), HD 175955, HD 182736, HD 185351, HD 188512 (β Aql), HD 189349. These stars were selected as possible candidates for benchmark stars that will be used for testing stellar models and validating large stellar surveys.

All stars were selected with collaboration with spectroscopy teams of large stellar surveys. The stars have sizes and grades of brightness that allow us to reliably measure their angular diameters using the chosen interferometer and, thereby, to derive

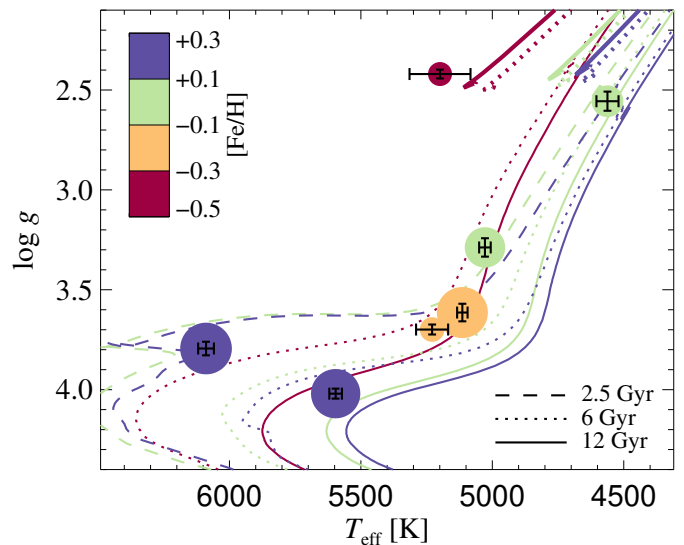


Fig. 1. Stellar parameters of our program stars, colour-coded by metallicity, compared to theoretical Dartmouth isochrones of different ages (linestyles), and with metallicities of $[\text{Fe}/\text{H}] = +0.2, 0.0$ and -0.5 (colours). Stellar evolution tracks for horizontal branch and AGB stars are overlaid based on the approximate RGB tip mass at each age and metallicity. Formal 1σ uncertainties are shown by the error bars. The symbol size is logarithmically proportional to the angular diameter of each star.

reliable values for T_{eff} . These giant and subgiant stars will be added to the first set of metal-poor stars and second set of dwarf stars from this programme by Karovicova et al. (2020) and Karovicova et al. (2021), respectively. The metallicities of our stars range between -0.6 and $+0.3$ dex. The stellar parameters of the seven giant and subgiant stars are listed in Table 1 and shown in Fig. 1.

All the stars in our giant and subgiant sample have previous interferometric observations. We discuss these previous measurements and compare them with our new measurements in Sect. 4.3. One of the stars, namely, HD 121370 (η Boo), is a current *Gaia*-ESO benchmark star. The star was interferometrically observed by Nordgren et al. (2001), Mozurkewich et al. (2003), Thévenin et al. (2005), van Belle et al. (2007), and Baines et al. (2014). The *Gaia*-ESO benchmark sample adopted the angular diameter measured by van Belle et al. (2007). We are revising the measurement of this *Gaia*-ESO benchmark in this study. We also present the measurements for five stars that have been proposed as future benchmarks in Heiter et al. (2015).

Three targets are in multiple systems, that is: HD 121370 (η Boo), HD 161797 (μ Her), and HD 188512 (β Aql). In particular, HD 121370 (η Boo) is a long-period spectroscopic binary with a separation of more than 115 arcsec from a faint companion that does not contribute to the flux in PAVO (Mason et al. 2001). Next, HD 161797 (μ Her) is a quadruplet system at a distance 8.3 pc. It consists of the G5IV primary and several M dwarfs (Roberts et al. 2016). The Ab component is separated by 1.8 arcsec, and the BC pair by 35 arcsec from the primary (Mason et al. 2001). All the components make a negligible contribution to the flux in PAVO. Finally, HD 188512 (β Aql) is a binary system. The companion, β Aql B, is a $V = 11.4$ mag M3 dwarf separated by approximately 13.4 arcsec (Mason et al. 2001) and it makes a negligible contribution to the flux.

Table 1. Stellar parameters.

Star		Sp.type	Right ascension	Declination	m_V (mag)	m_R (mag)	$E(B-V)$ (mag)	π
HD 121370	η Boo	G0IV	13 54 41.0789	+18 23 51.7946	2.68	2.24	0 ± 0	87.750 ± 1.240
HD 161797	μ Her	G5IV	17 46 27.5267	+27 43 14.4380	3.42	2.89	0 ± 0	119.110 ± 0.480
HD 175955		K0III	18 55 33.3265	+47 26 26.7847	7.02	7.02	0.01 ± 0.02	7.366 ± 0.030
HD 182736		G8IV	19 24 03.3794	+44 56 00.7352	7.01	7.02	0 ± 0	17.176 ± 0.025
HD 185351		G8.5III	19 36 37.9763	+44 41 41.7600	5.17	5.18	0 ± 0	24.225 ± 0.082
HD 188512	β Aql	G8IV	19 55 18.7926	+06 24 24.3425	3.71	3.05	0 ± 0	74.760 ± 0.360
HD 189349		G4III-IV	19 58 02.3822	+40 55 36.6322	7.31	7.32	0.02 ± 0.03	4.964 ± 0.340

Notes. Parallaxes are from *Gaia* DR2, without any zero point correction.

Table 2. Interferometric observations: Giants and subgiants.

Science target	UT date	Telescope	B (m)	# of obs.	Calibrator stars
HD 121370	2015 Apr. 28	E1E2	65.91	4	HD 116706, HD 121996
	2015 Apr. 29	E1E2	65.91	4	HD 116706, HD 121996
	2015 Apr. 30	E1E2	65.91	3	HD 116706, HD 121996
	2018 Aug. 5	E1E2	65.91	2	HD 116706, HD 121996
	2018 Aug. 7	E1E2	65.91	2	HD 121996
HD 161797	2015 Apr. 28	E1E2	65.91	2	HD 157087, HD 166230
	2015 Apr. 29	E1E2	65.91	2	HD 157087, HD 166230
	2015 Jun. 18	E1E2	65.91	2	HD 166230
HD 175955	2009 Jul. 15	S2W2	177.45	2	HD 179095, HD 180501, HD 184147
	2011 Jul. 3	W1W2	107.93	2	HD 174177
HD 182736	2009 Jul. 15	S2W2	177.45	1	HD 183142, HD 188461
	2009 Jul. 19	S2E2	248.13	1	HD 184147, HD 188461
	2010 Jul. 20	S2E2	248.13	1	HD 179483
	2011 Jul. 2	S1W1	278.50	2	HD 180681, HD 183142
HD 185351	2013 Jul. 7	W1W2	107.93	5	HD 177003, HD 185872, HD 188252
	2014 Apr. 6	W1W2	107.93	1	HD 185872
	2014 Apr. 7	W1W2	107.93	2	HD 177003, HD 185872
	2014 Apr. 10	E2W2	156.26	1	HD 184787, HD 188252
HD 188512	2015 Jul. 27	E1E2	65.91	3	HD 179761, HD 188385
	2016 Aug. 15	E2W2	156.26	1	HD 186689
	2016 Aug. 17	W1W2	107.93	4	HD 186689, HD 191263
HD 189349	2009 Jul. 14	S2W2	177.45	2	HD 188461, HD 190025
	2009 Jul. 15	S2W2	177.45	1	HD 188461
	2011 Jul. 5	S1W2	210.98	1	HD 189845

2.2. Interferometric observations and data reduction

We observed these stars using the Precision Astronomical Visible Observations (PAVO) interferometric instrument (Ireland et al. 2008) at the CHARA (Center for High Angular Resolution Astronomy) Array at Mt. Wilson Observatory, California (Ten Brummelaar et al. 2005). PAVO is operating as a pupil-plane beam combiner in optical wavelengths between ~ 630 – 880 nm. The CHARA Array offers the longest available baselines in the optical wavelengths worldwide, with baselines up to 330 m. The limiting magnitude of the observed targets is of $R \sim 7.5$. If the weather conditions allow, the limiting magnitude can be slightly extended up to $R \sim 8$.

The stars were observed using baselines between 65.91 m and 278.5 m. We collected the observations between 2015 Apr. 28 and 2018 Aug. 7. Additionally, four of our targets have been previously observed with PAVO between 2009–2013. These observations were reanalysed. This includes a new data reduc-

tion, so that all the presented data have been analysed consistently. This is mainly because in comparison to previous studies our treatment of limb-darkening differs. The previously published data include the observations of HD 175955, HD 182736, HD 189349 (Huber et al. 2012), and HD 185351 (Johnson et al. 2014). The dates of all observations, telescope configuration, and the baselines, B , are summarized in Table 2.

For the data reduction, we used the PAVO reduction software, which has been broadly tested, especially for single baseline squared visibility (V^2) observations, and has been previously used in multiple studies (e.g., Bazot et al. 2011; Derekas et al. 2011; Huber et al. 2012; Maestro et al. 2013). Within the data reduction software, we applied several visibility corrections. This includes a coherence time (t_0) correction. This correction is based on a ratio of coherent and incoherent visibility estimators and may be used to correct visibility losses. However, since it can introduce biases, it was not used consistently throughout the whole study. We note, however, that this correction may have been used

Table 3. Calibrator stars used for interferometric observations: Giants and subgiants.

Calibrator	Spectral type	m_V	m_K	UD (mas)
HD 116706	A3IV	5.75	5.50	0.271
HD 121996	A0V	5.75	5.70	0.239
HD 157087	A3III	5.36	5.14	0.320
HD 166230	A8III	5.10	4.61	0.419
HD 174177	A2IV	6.51	6.26	0.191
HD 177003	B2.5IV	5.38	5.90	0.204
HD 179095	A0	6.92	6.99	0.131
HD 179483	A2V	7.20	6.90	0.143
HD 179761	B7III	5.15	5.28	0.271
HD 180501	A0V	7.42	7.27	0.118
HD 180681	A0V	7.48	7.39	0.111
HD 183142	B8V	7.07	7.53	0.096
HD 184147	B9IV	7.17	7.16	0.122
HD 185872	B9III	5.40	5.48	0.268
HD 186689	A3IV	5.91	5.46	0.284
HD 188252	B2III	5.90	6.36	0.165
HD 188385	A2V	6.13	6.00	0.213
HD 188461	B2IV	6.99	7.45	0.098
HD 189845	A0	7.22	7.08	0.128
HD 190025	B5V	7.53	7.78	0.087
HD 191263	B3V	6.34	6.72	0.142

in the previous studies of HD 175955, HD 182736, HD 189349 (Huber et al. 2012), and HD 185351 (Johnson et al. 2014).

Additionally, we also changed the used wavelength range. In our study, we include all 38 channels, which range between 630 and 880 nm. In the previous studies, only the central 23 channels were used, ranging between 650 and 800 nm. The shorter range was used to avoid the possibly unreliable data towards the end of the range. We found our data was internally consistent within uncertainties, even though the edges of the bandpass typically had higher uncertainties, and, therefore, we included the full range. The absolute uncertainty on the wavelength scale was set to 5 nm.

In order to monitor the interferometric transfer function, a set of calibrating stars was observed immediately before and after the science targets. We selected the calibrating stars from the CHARA catalog of calibrators and from the Hipparcos catalogue (ESA 1997). The calibrating stars were selected to be either unresolved or nearly unresolved sources located close on sky to our science targets. We determined the angular diameters of the calibrators using the $V-K$ relation of Boyajian et al. (2014). We corrected for limb-darkening to determine the uniform disc diameter in the R band.

We used V -band magnitudes from the Tycho-2 catalogue (Høg et al. 2000). We converted them into the Johnson system using the calibration by Bessell (2000). We selected the K -band magnitudes from the Two Micron All Sky Survey (2MASS; Skrutskie et al. 2006). We estimated the reddening from the dust map of Green et al. (2015) and we applied the reddening law of O’Donnell (1994). The relative uncertainty on calibrator diameters was set to 5% (Boyajian et al. 2014), covering both the uncertainty on the calibrator diameters as well as the reddening.

All the calibrating stars were checked for binarity in *Gaia* DR2, the proper motion anomaly (Kervella et al. 2019), the phot_bp_rp_excess_factor (Evans et al. 2018), and the renormalised unit weight error (RUWE; Belokurov et al. 2020).

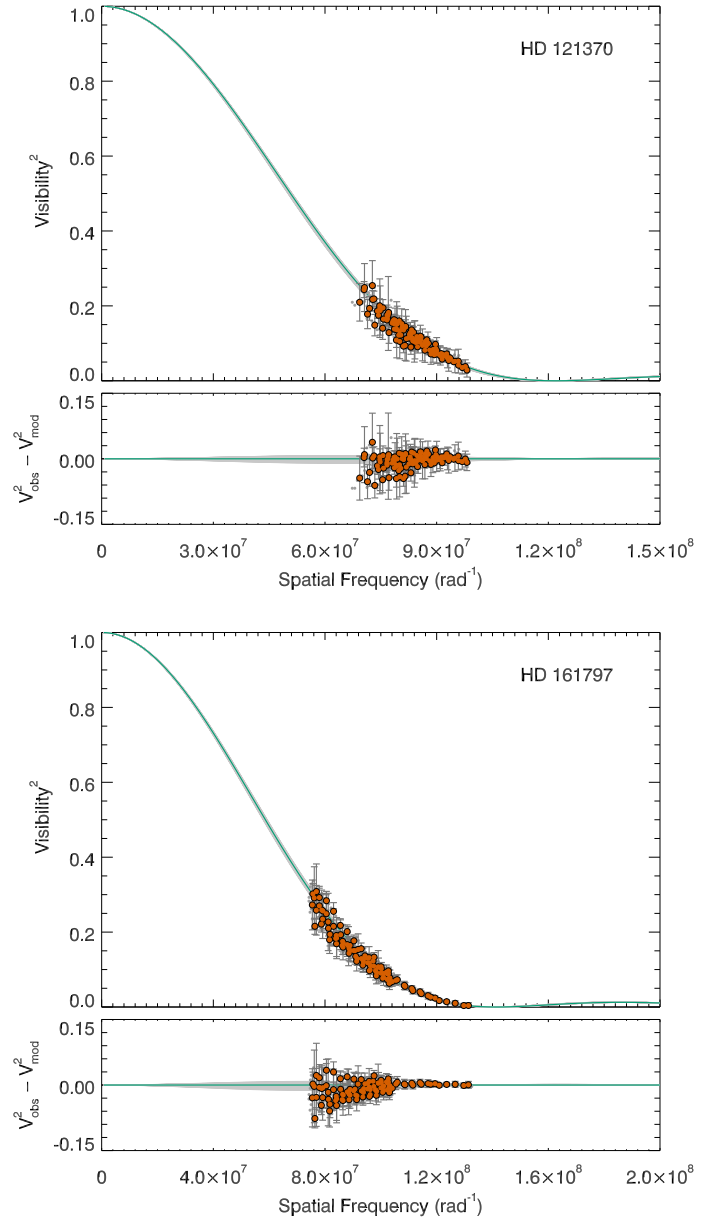


Fig. 2. Squared visibility vs. spatial frequency for HD 121370 and HD 161797. The HD number is noted in the right upper corner in the each plot. The raw error bars have been scaled to the reduced χ^2 before the final fitting. For HD 121370, the reduced $\chi^2 = 13.1$ and for HD 161797, $\chi^2 = 5.9$. The grey dots are the individual PAVO measurements in each wavelength channel. For clarity, we show weighted averages of the PAVO measurements as red circles. The green line shows the fitted limb-darkened model to the PAVO data, with the light grey-shaded region indicating the $1-\sigma$ uncertainties. Lower panel: residuals from the fit.

All these sources suggest that none of our calibrators have a companion that is large enough to affect our interferometric measurements or estimated calibrator sizes.

Since we noticed that using high-order limb-darkening coefficients to estimate of the calibrator sizes has a negligible impact ($\sim 0.3\%$) that is significantly smaller than our 5% uncertainty in the calibrator diameters, the angular sizes of the calibrators were estimated as a uniform disc in the R -band. The calibrating stars and their spectral type, magnitude in the V and R band, their expected angular diameter, and the corresponding science targets are summarized in Table 3.

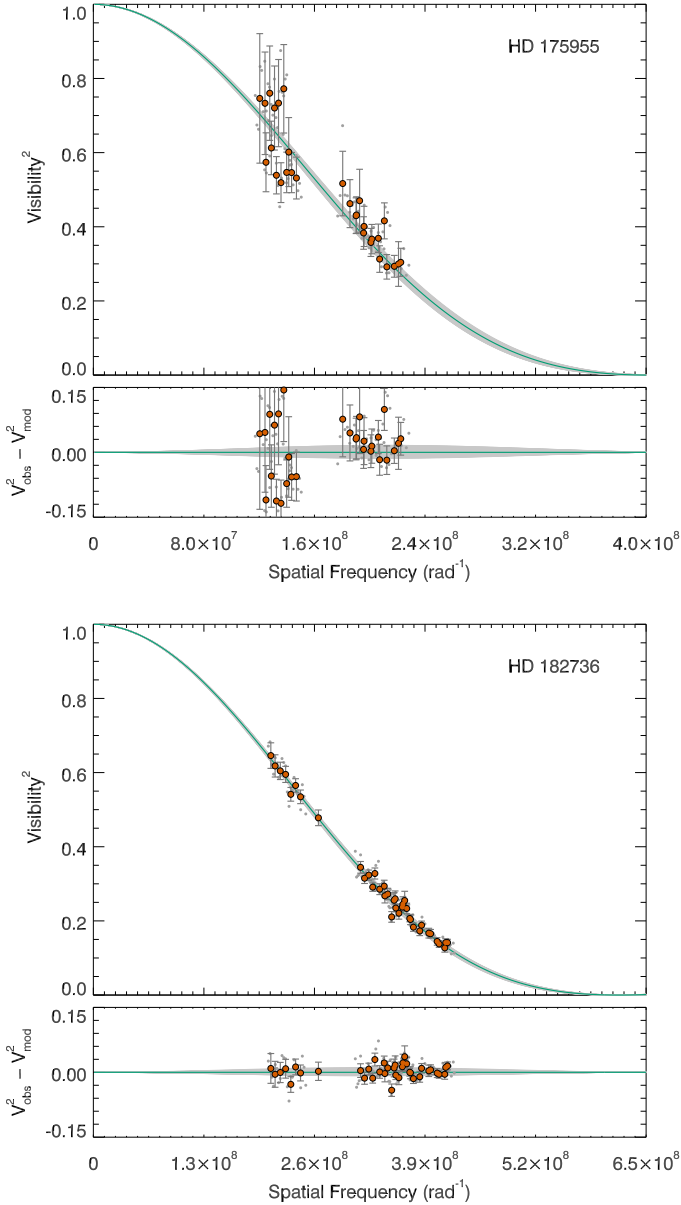


Fig. 3. Squared visibility vs. spatial frequency for HD 175955 and HD 182736. *Lower panel:* residuals from the fit. The error bars have been scaled to the reduced χ^2 . For HD 175955 the reduced $\chi^2 = 2.3$ and for HD 182736 $\chi^2 = 1.1$. All lines and symbols are the same as for Fig. 2.

2.3. Modelling of limb-darkened angular diameters

We fitted the calibrated fringe visibilities with a limb-darkened disc model. It is common in interferometric studies for a linearly limb-darkened disc model to be used, however, as in our previous studies (Karovicova et al. 2018, 2020), here we use the four-term non-linear limb-darkening law of Claret (2000):

$$\frac{I(\mu)}{I(1)} = 1 - \sum_k^4 a_k (1 - \mu^{k/2}). \quad (1)$$

Here, $I(\mu)$ is the intensity of the stellar disc at $\mu = \cos(\gamma)$, γ is the angle between the line-of-sight and the normal to a given point on the stellar surface, and a_k are the limb-darkening coefficients.

We use this higher order limb-darkening law because it provides a better fit to the centre-to-limb intensity profiles predicted by model atmospheres (e.g., Claret 2000; Magic et al. 2015). A

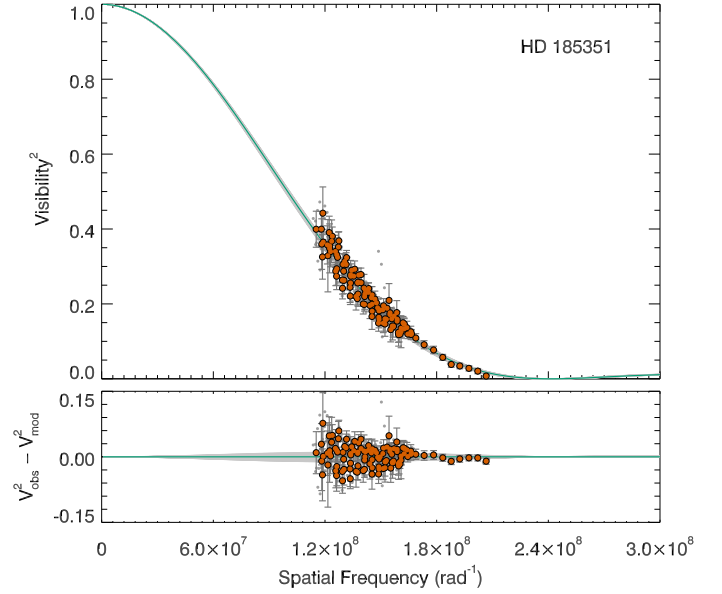


Fig. 4. Squared visibility vs. spatial frequency for HD 185351. *Lower panel:* residuals from the fit. The error bars have been scaled to the reduced χ^2 . The reduced χ^2 for HD 185351 is $\chi^2 = 4.8$. All lines and symbols are the same as for Fig. 2.

linear limb-darkening law, by contrast, tends to produce stronger limb-darkening across most of the disc than is warranted because it is not able to fit both the precipitous drop in intensity towards the limb and the more gradual decrease in intensity elsewhere.

Following the fringe visibility for a generalized polynomial limb-darkening law (Quirrenbach et al. 1996), the fringe visibilities for the four-term non-linear limb-darkening model are given by

$$V = \left(\frac{1 - \sum_k a_k}{2} + \sum_k \frac{2a_k}{k+4} \right)^{-1} \times \left[\left(1 - \sum_k a_k \right) \frac{J_1(x)}{x} + \sum_k a_k 2^{k/4} \Gamma\left(\frac{k}{4} + 1\right) \frac{J_{k/4+1}(x)}{x^{k/4+1}} \right], \quad (2)$$

where $x = \pi B \theta \lambda^{-1}$, with B the projected baseline, θ the angular diameter, $\Gamma(z)$ is the gamma function, and $J_n(x)$ is the n th-order Bessel function of the first kind. The quantity $B \lambda^{-1}$ is the spatial frequency. The squared visibilities versus spatial frequencies along with the residuals from the fit are shown in Figs. 2–5.

As for our previous studies, we determined the limb-darkening coefficients from the STAGGER grid of ab initio 3D hydrodynamic stellar model atmosphere simulations (Magic et al. 2013). We determined the coefficients for each model in the grid by fitting Eq. (1) to the μ -dependent synthetic fluxes calculated by Magic et al. (2015) in each of the 38 wavelength channels of PAVO. We interpolated within this grid to determine the coefficients for each star. These limb-darkening coefficients are given in Tables A.1 through A.7, available at the CDS. In the appendix, we include one table for one of the stars as an example. For ease of comparison with previous studies, we also provide angular diameter values determined using a linear limb-darkened law, with coefficients determined from the grid of Claret & Bloemen (2011) in Table 4. The limb-darkened diameters based on the STAGGER-grid are listed in Table 5 showing our final limb-darkened diameters using higher order limb-darkening model.

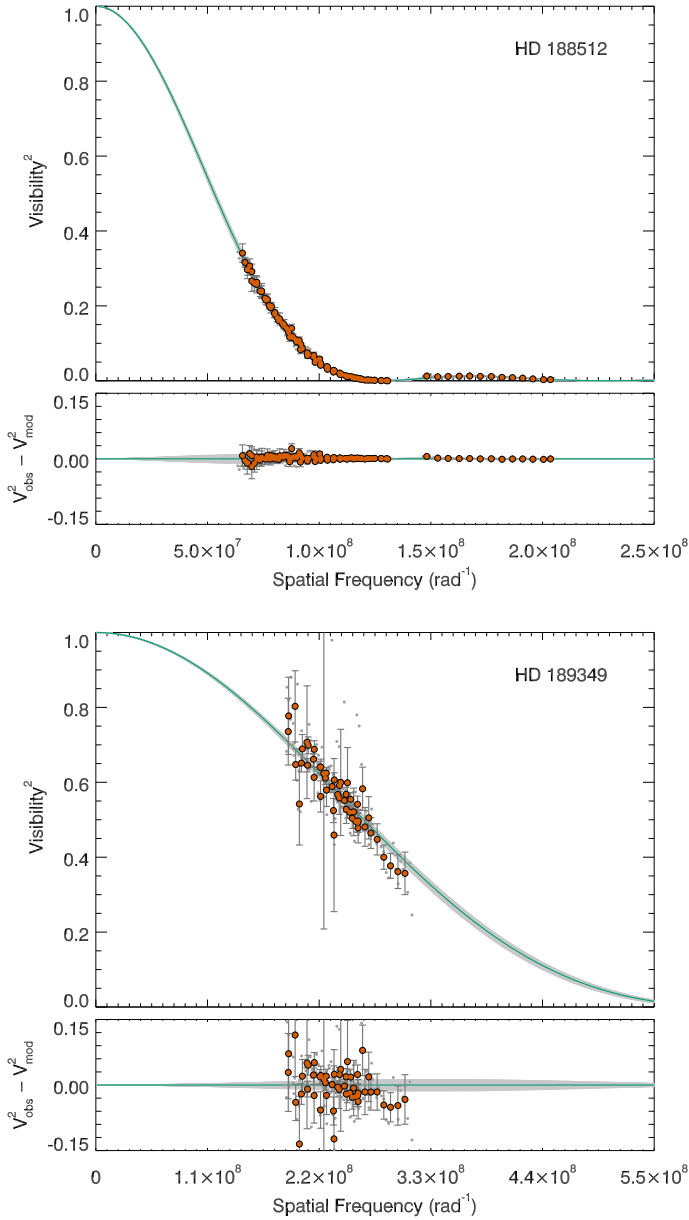


Fig. 5. Squared visibility vs. spatial frequency for HD 188512 and HD 189349. *Lower panel:* residuals from the fit. The error bars have been scaled to the reduced χ^2 . For HD 188512, the reduced $\chi^2 = 2.6$ and for HD 189349 $\chi^2 = 1.5$. All lines and symbols are the same as for Fig. 2.

Table 4. Angular diameters and linear limb-darkening coefficients.

Star	θ_{UD} (mas)	Linear limb-darkening ^(a)	
		u	θ_{LD} (mas)
HD 121370	2.088 ± 0.015	0.551 ± 0.012	2.206 ± 0.018
HD 161797	1.797 ± 0.015	0.605 ± 0.013	1.913 ± 0.016
HD 175955	0.632 ± 0.009	0.706 ± 0.010	0.678 ± 0.010
HD 182736	0.412 ± 0.004	0.621 ± 0.012	0.438 ± 0.004
HD 185351	1.057 ± 0.009	0.652 ± 0.011	1.129 ± 0.009
HD 188512	1.979 ± 0.018	0.633 ± 0.012	2.125 ± 0.016
HD 189349	0.401 ± 0.005	0.596 ± 0.013	0.423 ± 0.005

Notes. ^(a)Limb-darkening coefficients derived from the grid of Claret & Bloemen (2011); see text for details. The final limb-darkened diameters using higher order limb-darkening model are listed in Table 5.

3. Methods

3.1. Bolometric flux

Bolometric fluxes and associated uncertainties were derived with the exact same procedure described in Karovicova et al. (2020). Briefly, we adopted an iterative procedure to interpolate over the tables of bolometric corrections¹ of Casagrande & Vandenberg (2014, 2018). We used HIPPARCOS H_p and Tycho2 $B_T V_T$ magnitudes for all stars, and 2MASS JHK_S only when the quality flag was ‘A’. The adopted bolometric corrections are listed in Table 6, and already take reddening into account for stars affected by it (see Table 1 for the adopted $E(B-V)$ values).

Uncertainties in bolometric fluxes are obtained running a Monte Carlo simulation and taking into account the variance of different bands. Uncertainties for all stars amount to $\sim 2\%$ at most, with the exception of HD 189349, which reaches almost 9%. This uncertainty is driven by the scatter of bolometric corrections in different filters. Whether this is indicative of model inaccuracies, a wrong reddening estimate, or both is not possible to say, but it raises a warning about the feasibility of using this star as a benchmark.

While we do not take into account inaccuracies in model fluxes, a comparison with absolute spectrophotometry indicates that by using multiple bands, bolometric fluxes from the CALSPEC library can be recovered at a 1% level for FG stars (Casagrande & Vandenberg 2018). Our sample, however, comprises cooler stars, for which the performances of our bolometric corrections are much less tested (see e.g., discussions in White et al. 2018; Rains et al. 2021; Tayar et al. 2020). An encouraging comparison with the absolute spectrophotometry of a few GK subgiants in White et al. (2018) indicates that reliable fluxes can still be obtained from our bolometric corrections. Also, a given percentage change in bolometric flux carries a percentage change in effective temperatures that is four times smaller.

3.2. Stellar evolution models

We used the ELLI package² (Lin et al. 2018) together with Dartmouth stellar evolution tracks (Dotter et al. 2008) to determine stellar masses. The stellar evolution models were computed with alpha enhancement for the metal-poor stars, and are truncated at the RGB tip. The code produces an initial guess from a maximum likelihood estimate when comparing isochrones to the observed T_{eff} , $\log L/L_{\odot}$ and $[\text{Fe}/\text{H}]$. A Markov chain Monte Carlo (MCMC) method is then used to sample the posterior distribution of the stellar mass and age, assuming that errors on the observed quantities are uncorrelated. We take the mean and standard deviation of this distribution as our mass estimate. We then compute the surface gravity from the fundamental relation, rewritten in the form:

$$\log g = \log \frac{GM}{R^2} = \log \frac{4GM\varpi^2}{\theta^2}, \quad (3)$$

where G is the gravitational constant and ϖ is the parallax.

For three stars, namely, HD 175955, HD 189349, and HD 185351, the MCMC approach produced a posterior distribution that did not match the observed parameters well. For two of the stars, HD 175955 and HD 185351, we instead selected the mass that best reproduced the observations, in the sense that it maximized the likelihood function. We adopted a representative

¹ <https://github.com/casaluca/bolometric-corrections>

² Available online at <https://github.com/dotbot2000/elli>

Table 5. Observed (θ_{LD}) and derived (F_{bol} , M , L , R) stellar parameters.

Star	θ_{LD} (mas)	F_{bol} ($\text{erg s}^{-1} \text{cm}^{-2} 10^{-8}$)	$M(M_{\odot})$	$L(L_{\odot})$	$R(R_{\odot})$
HD 121370	2.173 ± 0.018	216.552 ± 2.065	1.61 ± 0.11	8.758 ± 0.261	2.659 ± 0.044
HD 161797	1.888 ± 0.014	116.485 ± 0.721	1.11 ± 0.06	2.557 ± 0.026	1.704 ± 0.016
HD 175955	0.661 ± 0.009	6.345 ± 0.156	1.23 ± 0.12	36.417 ± 0.941	9.796 ± 0.137
HD 182736	0.433 ± 0.009	4.672 ± 0.102	1.34 ± 0.05	4.932 ± 0.109	2.711 ± 0.019
HD 185351	1.113 ± 0.009	26.396 ± 0.175	1.73 ± 0.17	14.008 ± 0.133	4.946 ± 0.043
HD 188512	2.096 ± 0.014	100.053 ± 0.738	1.36 ± 0.13	5.575 ± 0.068	3.012 ± 0.025
HD 189349	0.417 ± 0.005	4.242 ± 0.366	0.73 ± 0.03	53.608 ± 4.686	9.084 ± 0.125

Notes. F_{bol} and L are obtained adopting $L_{\odot} = 3.842 \times 10^{33} \text{ erg s}^{-1}$.

Table 6. Bolometric corrections.

Star	BC_{H_p}	BC_{B_T}	BC_{V_T}	BC_J	BC_H	BC_K	B_T	eB_T	V_T	eV_T	H_p	eH_p	J	eJ	H	eH	K	eK
HD 121370	-0.115	-0.697	-0.055	1.016	1.234	1.318	3.380	0.014	2.719	0.009	2.7957	0.0004	-	-	-	-	-	-
HD 161797	-0.207	-0.984	-0.146	1.180	1.481	1.580	4.336	0.014	3.490	0.009	3.5596	0.0005	-	-	-	-	-	-
HD 175955	-0.648	-1.982	-0.618	1.482	2.056	2.209	8.513	0.016	7.146	0.010	7.1808	0.0010	4.999	0.024	-	-	4.318	0.017
HD 182736	-0.313	-1.169	-0.259	1.276	1.673	1.775	8.021	0.016	7.103	0.010	7.1673	0.0009	5.515	0.024	-	-	5.028	0.016
HD 185351	-0.372	-1.369	-0.316	1.345	1.775	1.893	6.350	0.014	5.273	0.009	5.3355	0.0005	-	-	-	-	-	-
HD 188512	-0.350	-1.257	-0.298	1.312	1.736	1.844	4.789	0.014	3.807	0.009	3.8668	0.0004	-	-	-	-	-	-
HD 189349	-0.407	-1.229	-0.358	1.251	1.675	1.778	8.411	0.016	7.411	0.010	7.4738	0.0011	5.638	0.024	5.181	0.021	5.124	0.029

Notes. Adopted bolometric corrections (BC). HIPPARCOS H_p and *Tycho2* $B_T V_T$ magnitudes for all stars. 2MASS JHK_S only if the quality is flag 'A'. The zero-point of these bolometric corrections is set by $M_{\text{bol},\odot} = 4.75$. F_{bol} for each star is obtained from Eq. (3) of Casagrande & Vandenberg (2018), adopting $L_{\odot} = 3.842 \times 10^{33} \text{ erg s}^{-1}$.

error estimate of 10% for these stars. The third star, HD 189349, is unusually warm relative to other red giant branch stars of similar luminosity, indicating a very low age (or high mass). Indeed, asteroseismology indicates that this star is undergoing core helium burning (HeB) and thus belongs to the red clump (RC) rather than the red giant branch (Takeda & Tajitsu 2015). Comparison to horizontal branch (HB) evolution tracks yields a fair match for $M = 0.9 \pm 0.1 M_{\odot}$, as opposed to the RGB solution $M = 2.1 \pm 0.2 M_{\odot}$. For this star, we opt instead for the asteroseismic surface gravity: adopting $\nu_{\text{max}} = 29.03 \pm 0.52 \mu\text{Hz}$ from Yu et al. (2018), we derive $\log g = 2.388 \pm 0.009$ using the scaling relation

$$\frac{g}{g_{\odot}} = \frac{\nu_{\text{max}}}{\nu_{\text{max},\odot}} \left(\frac{T_{\text{eff}}}{T_{\text{eff},\odot}} \right)^{3/2}. \quad (4)$$

For completeness, we also use a scaling relation from Kjeldsen & Bedding (1995),

$$\frac{M}{M_{\odot}} = \frac{\nu_{\text{max}}}{\nu_{\text{max},\odot}} \sqrt{\frac{T_{\text{eff}}}{T_{\text{eff},\odot}}} \left(\frac{R}{R_{\odot}} \right)^2, \quad (5)$$

to derive the seismic mass, $M = 0.728 \pm 0.025$, but we note that the surface gravity for this star has been derived directly, yielding smaller error bars thanks to the cancellations of terms.

3.3. Spectroscopic analysis

High-resolution spectra for the stars were extracted from the ELODIE ($R \approx 42\,000$, Moultaika et al. 2004) and FIES ($R \approx 65\,000$, Telting et al. 2014) archives. We determined the stellar iron abundances using a custom pipeline based on the spectrum synthesis code SME (Piskunov & Valenti 2017) using MARCS

model atmospheres (Gustafsson et al. 2008) and pre-computed non-LTE departure coefficients for Fe (Amarsi et al. 2016).

We selected unblended lines of Fe I and Fe II between 4400 and 6800 Å with accurately known oscillator strengths from laboratory measurements. For saturated lines, we ensured that collisional broadening parameters were available from ABO theory (Barklem et al. 2000; Barklem & Aspelund-Johansson 2005). Abundances were also measured from solar spectra recorded with the same spectrographs as our target stars, based on observations of light reflected off the Moon (ELODIE) and Vesta (FIES). We thereby produce solar-differential abundances, which mostly cancels uncertainties in oscillator strengths as well as potential systematic differences between the spectrographs. We estimated the iron abundance of each star from the outlier-resistant mean with 3σ clipping. We also report the difference in abundance between lines of Fe I and Fe II as an estimate of how closely our fundamental stellar parameters fulfill the ionization equilibrium. Finally, we compute a systematic uncertainty on the metallicity, which we derive by perturbing the input parameters one at a time according to their formal errors, and we add these differences in quadrature.

4. Results and discussion

4.1. Recommended stellar parameters

In this section, we present angular diameters and fundamental stellar parameters for a set of seven giant and subgiant stars: HD 121370 (η Boo), HD 161797 (μ Her), HD 175955, HD 182736, HD 185351, HD 188512 (β Aql), and HD 189349. Six of these stars have been recommended as benchmark stars. The radius and mass are estimated from measurements of θ_{LD} , F_{bol} and parallax. All the values are summarised, along with their luminosity, in Table 5. The final fundamental stellar parameters

Table 7. Derived stellar parameters (T_{eff} , $\log g$, [Fe/H]).

Star	T_{eff} (K)	$\log g$ (dex)	[Fe/H] (dex)
HD 121370	6090 ± 29	3.794 ± 0.034	0.29 ± 0.07
HD 161797	5596 ± 22	4.020 ± 0.025	0.26 ± 0.04
HD 175955	4568 ± 42	2.556 ± 0.048	0.00 ± 0.13
HD 182736	5229 ± 37	3.699 ± 0.025	-0.18 ± 0.04
HD 185351	5025 ± 22	3.288 ± 0.046	-0.02 ± 0.07
HD 188512	5113 ± 20	3.614 ± 0.044	-0.20 ± 0.04
HD 189349	5199 ± 116	2.388 ± 0.009	-0.57 ± 0.09

of T_{eff} , $\log g$, and [Fe/H] are listed in Table 7 and also discussed below.

4.2. Uncertainties

The desired precision requested by the spectroscopic teams such as *Gaia*-ESO or GALAH is around 1% (or around 40–60 K). We show that for the stars in our sample the uncertainties in T_{eff} are less than 50 K (or less than 1%), with the exception of HD 189349, which we do not recommend as a benchmark. The uncertainty for this star is 2% and it is dominated by uncertainties in bolometric flux. Overall, the errors in T_{eff} for stars in our sample resulting from uncertainties in the limb-darkened angular diameters are at most 31 K, with a median of just 24 K (0.5%).

The final uncertainties in T_{eff} consist of the uncertainties in the bolometric flux and the uncertainties in the angular diameter. We present the contributions from each measurement independently in Table 8. For clarity, the dominating uncertainty is highlighted in boldface. The presented uncertainties have been computed by artificially setting the uncertainties from the other measurement to zero. We note that in the final error estimates of T_{eff} , we propagate the statistical measurement uncertainties in $\log g$ and [Fe/H] from the isochrone fitting and spectroscopic analysis and fold them into the uncertainties in the angular diameters. The median uncertainties in $\log g$ and [Fe/H] across our sample of stars are 0.034 dex and 0.07 dex, respectively (for details, see Table 7).

4.3. Comparison with angular diameter values in the literature

All stars in our sample have been previously interferometrically observed and their angular diameters reported in the literature. We conducted new observations for some of the stars. In addition, for all stars we carried out a fresh data reduction and analysis of the data applying our updated analysis and updated treatment of limb-darkening. We list our measurements of angular diameters, θ_{LD} , together with values reported in the literature in Table 9. We compare the presented values in Fig. 6.

HD 121370 (η Boo). We conducted new observations of this star and measured angular diameter as $\theta_{\text{LD}} = 2.173 \pm 0.018$ mas. The star was previously observed using various interferometric instruments in several studies (see Table 9). This target is already in use as a benchmark. The *Gaia*-ESO benchmark team (Jofré et al. 2015) adopted the angular diameter measured by van Belle et al. (2007). Our value is in agreement within the uncertainties with this value. The largest disagreement between our θ_{LD} and the other measurements is found for the Mk. III measurement by Mozurkewich et al. (2003), which differs by 3σ .

Table 8. Uncertainties in T_{eff} and how they propagate from the underlying measurements.

Star	T_{eff} (K)	eT_{eff} (K)	eT_{eff} (%)	$eF_{\text{bol}}^{(a)}$ (K)	$e\theta_{\text{LD}}^{(b)}$ (K)
HD 121370	6090	29	0.5	15	25
HD 161797	5596	22	0.4	9	21
HD 175955	4568	42	0.9	28	31
HD 182736	5229	37	0.7	29	24
HD 185351	5025	22	0.4	8	20
HD 188512	5113	20	0.4	9	17
HD 189349	5199	116	2.2	112	31

Notes. ^(a)The uncertainties contribution from the bolometric flux if the θ_{LD} uncertainties are set to 0. ^(b)The uncertainties arising entirely from the angular diameter measurements if the F_{bol} uncertainties are set to 0. The dominating uncertainty is highlighted in boldface.

HD 161797 (μ Her). We measured the angular diameter of this star as $\theta_{\text{LD}} = 1.888 \pm 0.0014$ mas. This star was previously observed by Mozurkewich et al. (2003) with the Mk. III interferometer, who reported a value of $\theta_{\text{LD}} = 1.953 \pm 0.0039$ mas. It has also been observed with NPOI by Baines et al. (2014), who found $\theta_{\text{LD}} = 1.957 \pm 0.0012$ mas, and Baines et al. (2018), who found $\theta_{\text{LD}} = 1.880 \pm 0.0008$ mas. Our measurement agrees with the latter measurement. This star was suggested as a possible benchmark star in Heiter et al. (2015).

HD 175955. For this star, we report $\theta_{\text{LD}} = 0.661 \pm 0.009$ mas. This data was previously observed by Huber et al. (2012) with the PAVO instrument. These authors reported $\theta_{\text{LD}} = 0.680 \pm 0.01$ mas, having fitted the data with a linearly limb-darkened disc model, with the limb-darkening coefficient determined from the grid calculated by Claret & Bloemen (2011) based on 1D ATLAS models. This star has also been suggested as a possible benchmark star. Therefore, for consistency, we carried out a fresh data reduction and reanalysed this data with limb-darkening coefficients from 3D model atmospheres, using a higher-order limb-darkening model. In this case, our angular diameter differs in comparison to Huber et al. (2012) by 1.4σ . This can be attributed with the changes in our fresh data reduction. We discuss the impact of the fresh reduction of the PAVO data in more detail below.

HD 182736. We measured the angular diameter of this star as $\theta_{\text{LD}} = 0.433 \pm 0.0009$ mas. The same data was also previously analysed by Huber et al. (2012), who reported $\theta_{\text{LD}} = 0.436 \pm 0.005$ mas, which agrees with our value. Because this star was suggested as a possible benchmark star, we reanalysed the data applying limb-darkening coefficients from 3D model atmospheres and using a higher-order limb-darkening model.

HD 185351. For this star, we report $\theta_{\text{LD}} = 1.113 \pm 0.009$ mas. We again reanalysed PAVO data observed by Johnson et al. (2014), who reported $\theta_{\text{LD}} = 1.133 \pm 0.0013$ mas. Johnson et al. (2014) also reported observations with the Classic *H* instrument at CHARA, finding $\theta_{\text{LD}} = 0.120 \pm 0.018$ mas. Our value agrees within uncertainties with the Classic *H* measurement, but differs from the measurement based on the PAVO data by 1.3σ . Again, this can be attributed with the changes in our fresh data reduction, discussed in more detail below.

HD 188512 (β Aql). We new observations of this star and report an angular diameter of $\theta_{\text{LD}} = 2.096 \pm 0.014$ mas. This star was previously observed with NPOI by Nordgren et al. (1999)

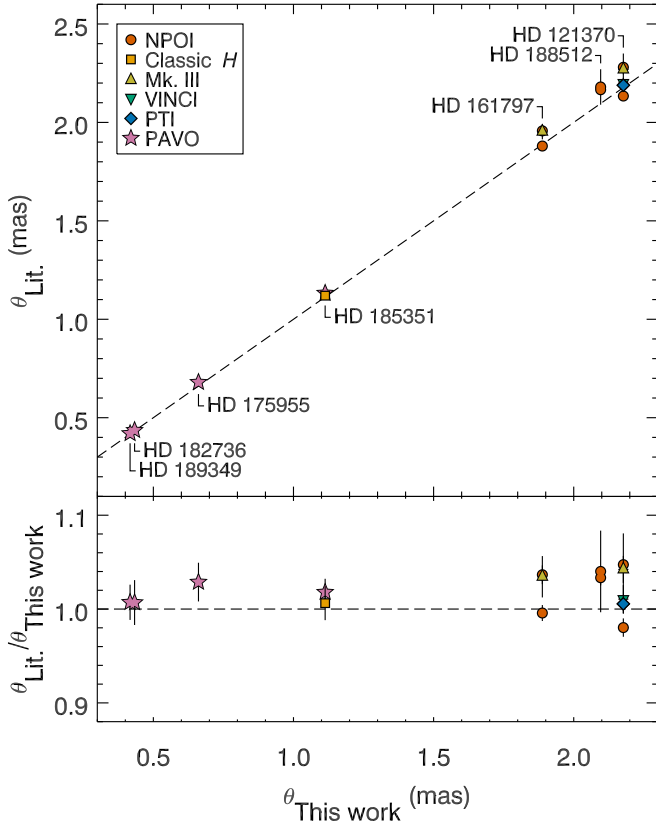


Fig. 6. Comparison of limb-darkened angular diameters from the literature with measurements from this work. Symbols correspond to the beam combiner used for the literature measurement: NPOI (red circle), CHARA Classic in the H band (orange square), Mark III (yellow triangle), VLTI/VINCI (green triangle), PTI (blue diamond), and PAVO (pink stars).

and Baines et al. (2014). Nordgren et al. (1999) reported $\theta_{\text{LD}} = 2.18 \pm 0.09$ mas and Baines et al. (2014) reported $\theta_{\text{LD}} = 2.166 \pm 0.009$ mas. Our measurement agrees with that of Nordgren et al. (1999), although that measurement has a large uncertainty. There is, however, a 4.2σ disagreement with the value found by Baines et al. (2014). For this star, we collected very high quality data, fully resolving the star and covering the visibility curve into the second lobe, thus offering a high level of reliability to our measurement. A detailed analysis of the data covering the second lobe of the visibility function is beyond the scope of this study and will be addressed in a later paper. This star has been suggested as a possible benchmark star (Heiter et al. 2015).

HD 189349. We measured the angular diameter of this star to be $\theta_{\text{LD}} = 0.417 \pm 0.005$ mas. These PAVO data were previously analysed by Huber et al. (2012), who reported $\theta_{\text{LD}} = 0.420 \pm 0.006$ mas. Because the star was suggested as a possible benchmark star, we reanalysed it here for consistency. We find that the angular diameter measurements are in good agreement. While this star was recommended as a benchmark by Heiter et al. (2015), at this moment we do not recommend this star as a potential benchmark due to its uncertain bolometric flux and, subsequently, its uncertain T_{eff} values (see Sect. 3.1).

Our fresh reduction of the previously published PAVO data had only a minimal impact on the determined angular diameters. Potential differences in the reductions that could have had an impact include making different choices for data cuts based on signal-to-noise ratio (S/N) and other metrics, while

also using new calculations of calibrator sizes. In some cases, our choice not to use the t_0 correction (as described in Sect. 2.2) can have a more significant impact. Additionally, we used all 38 of the PAVO wavelength channels, whereas the previous studies only used the central 23 channels between 650 and 800 nm. The effect of these data reduction changes alone can be determined by comparing the linear limb-darkened diameters given in Table 4 with the diameters reported in the literature. The diameters in Table 4 agree (within 1σ) with the literature values.

The remaining difference between our final adopted angular diameters and the literature values for these targets is attributed to the updated limb-darkening treatment. The previous PAVO studies fitted the data using a linear limb-darkening model, with coefficients calculated from 1D ATLAS model atmospheres by Claret & Bloemen (2011). A single coefficient for the R -band was used across all wavelength channels. As discussed in detail by Karovicova et al. (2021), the combined effect of this was that the adopted coefficients implied stronger limb-darkening than justified by the model atmospheres. As a consequence, the previous angular diameters were too large and, on average, our final adopted angular diameters are 1.5% smaller.

4.4. Spectroscopic analysis

Our iron abundance determinations from lines of neutral and ionised iron yield very good agreement, as illustrated in Fig. 7. The abundance differences are small, consistent with zero, for all stars except HD 189349. This star, which has the lowest metallicity in the sample, and is also the only core helium-burning star, shows a positive deviation of 0.2 dex.

Errors in stellar parameters have different impact on lines of neutral and singly ionized iron. The sensitivity is such that a deviation from ionization equilibrium of 0.05 dex may correspond to an error of approximately 50 K in T_{eff} , or 0.10 dex in $\log g$. The excellent agreement for all but one stars in our sample therefore indicate that our error estimates are realistic, and that no significant systematics are present. For HD 189349, the larger deviation by 0.2 dex may indicate either an error in its temperature by upwards of 200 K, an error in $\log g$ by as much as 0.4 dex, or issues related to spectroscopic modelling (see e.g., Lebzelter et al. 2012).

4.5. Comparison with asteroseismology

Each of our targets exhibits solar-like oscillations that are stochastically excited and damped by convection. Measurements of the oscillation frequencies can place tight constraints on the interior structure of a star, and can be used to infer stellar properties including the radius. Here, we briefly compare our interferometric radii with radii derived from asteroseismic studies in the literature.

Three of our targets have been the subject of ground-based radial velocity campaigns to detect their oscillations: HD 121370 (η Boo; Kjeldsen et al. 2003; Carrier et al. 2005), HD 161797 (μ Her; Bonanno et al. 2008; Grundahl et al. 2017), and HD 188512 (β Aql; Corsaro et al. 2012). The other four stars were observed by the Kepler mission. HD 175955, HD 182736, and HD 189349 were studied by Huber et al. (2012). Additionally, HD 175955 and HD 189349 were amongst the 16000 red giants in the sample of Yu et al. (2018). Also, HD 185351 was one of the brightest stars observed during the nominal Kepler mission and its oscillations were studied by Johnson et al. (2014).

Table 9. Prior angular diameters.

Star	Our value (mas)	Literature value (mas)	Reference	Instrument
HD 121370	2.173 ± 0.018	2.28 ± 0.07	Nordgren et al. (2001)	NPOI
		2.269 ± 0.025	Mozurkewich et al. (2003)	Mk. III
		2.200 ± 0.027	Thévenin et al. (2005)	VLTI/VINCI
		2.189 ^{+0.006} _{-0.014}	van Belle et al. (2007)	PTI
		2.134 ± 0.012	Baines et al. (2014)	NPOI
HD 161797	1.888 ± 0.014	1.953 ± 0.039	Mozurkewich et al. (2003)	Mk. III
		1.957 ± 0.012	Baines et al. (2014)	NPOI
		1.880 ± 0.008	Baines et al. (2018)	NPOI
HD 175955	0.661 ± 0.009	0.68 ± 0.01	Huber et al. (2012)	CHARA/PAVO
HD 182736	0.433 ± 0.009	0.436 ± 0.005	Huber et al. (2012)	CHARA/PAVO
HD 185351	1.113 ± 0.009	1.120 ± 0.018	Johnson et al. (2014)	CHARA/Classic H
		1.133 ± 0.013	Johnson et al. (2014)	CHARA/PAVO
HD 188512	2.096 ± 0.014	2.18 ± 0.09	Nordgren et al. (1999)	NPOI
		2.166 ± 0.009	Baines et al. (2014)	NPOI
HD 189349	0.417 ± 0.005	0.420 ± 0.006	Huber et al. (2012)	CHARA/PAVO

The simplest way to determine masses and radii from asteroseismic measurements is to exploit scaling relations for two quantities that parameterise the observed oscillation spectrum. The frequency at which the oscillation amplitude peaks, ν_{\max} , is observed to scale as follows (Brown et al. 1991; Kjeldsen & Bedding 1995):

$$\frac{\nu_{\max}}{\nu_{\max,\odot}} \approx \left(\frac{M}{M_{\odot}}\right) \left(\frac{R}{R_{\odot}}\right)^{-2} \left(\frac{T_{\text{eff}}}{T_{\text{eff},\odot}}\right)^{-1/2}. \quad (6)$$

The large frequency separation, $\Delta\nu$, between modes of the same angular degree and consecutive radial order scales as (Ulrich 1986):

$$\frac{\Delta\nu}{\Delta\nu_{\odot}} \approx \left(\frac{M}{M_{\odot}}\right)^{1/2} \left(\frac{R}{R_{\odot}}\right)^{-3/2}. \quad (7)$$

Combining these two relations with the known T_{eff} allows the mass and radius to be determined directly (e.g., Kallinger et al. 2010). Comparisons with independent measurements have found radii determined from the scaling relation to be accurate to $\sim 5\%$ (e.g., Huber et al. 2012, 2017; White et al. 2013; Brogaard et al. 2018). However, as the scaling relations rely on a number of assumptions, including that the stars are homologous to the Sun, deviations arise for stars that have significantly different structures, such as red giants. These deviations have been investigated, particularly for the $\Delta\nu$ scaling relation, which has a more established theoretical basis, and corrections to improve the relations have been proposed (e.g., White et al. 2011; Guggenberger et al. 2016; Sharma et al. 2016; Rodrigues et al. 2017; Viani et al. 2017).

Figure 8 shows the scaling relation radii compared to the interferometric radii for our sample. The uncorrected scaling relation radii are typically accurate to better than 10% for this sample. The scaling relation radii for HD 121370 and

HD 188512 are relatively uncertain, owing to the comparatively short length and lower signal-to-noise ratio of the ground-based data for these stars. Two of the giants observed by Kepler, HD 185351 and HD 175955, have an uncorrected scaling relation radius that disagrees with the interferometric radius, the latter by 3σ . The scaling relation radii corrected using the $\Delta\nu$ corrections of Sharma et al. (2016) show better agreement with the interferometric radii in general, and for these two stars, in particular. This provides further support for the use of such corrections. It is only for one star, HD 161797, that the correction does indeed worsen the agreement with the interferometric radius significantly.

A more rigorous method of determining stellar parameters from asteroseismology than using scaling relations is detailed stellar modelling using the observed oscillation frequencies. Three of these stars have been the subject of such efforts. As one of the first stars to have solar-like oscillations detected, HD 121370, has been studied in detail (e.g., Christensen-Dalsgaard et al. 1995; Di Mauro et al. 2003; Carrier et al. 2005; Straka et al. 2006). However, these studies did not report a final value for the radius with uncertainties. The radius of the best fitting model found by Carrier et al. (2005) is $2.72 R_{\odot}$, which is in better agreement with the interferometric radius than the scaling relation radii. Li et al. (2019) modelled HD 161797, however, they used the interferometric radius as one of the constraints on their models, so a valid comparison cannot be made with their results. Finally, HD 185351 was modelled by Hjorringgaard et al. (2017), who sought to resolve tension between the interferometric and asteroseismic constraints by varying the input physics of the models; in particular, the convective core overshooting and mixing length parameter. Their radius, shown in Fig. 8, agrees well with our interferometric radius. More detailed modelling of more stars with both asteroseismic and interferometric constraints ought to allow for the

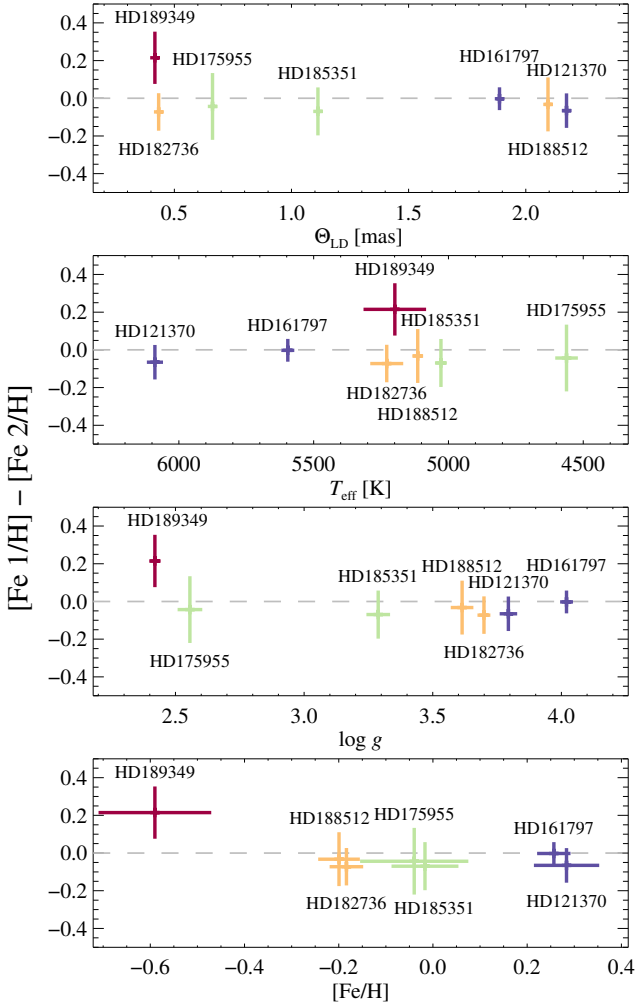


Fig. 7. Deviations from ionisation equilibrium, that is, the difference between the abundances determined from lines of neutral and ionised iron as a function of the measured stellar parameters. Vertical and horizontal lines represent the combined uncertainties from the two measurements. Stars are colour-coded according to metallicity, as shown in the bottom plot.

calibration of the input physics of models, such as convection (e.g., Joyce & Chaboyer 2018).

5. Conclusions

We presented a sample of giant and subgiant stars with highly accurate and reliable fundamental stellar parameters, extending the sample of stars that may be used as benchmarks for large stellar surveys. This is the third in a series of papers with this scientific goal. The sample in this paper consists of HD 121370 (η Boo), HD 161797 (μ Her), HD 175955, HD 182736, HD 185351, HD 188512 (β Aql), and HD 189349. One of these stars, HD 121370, is already listed as a *Gaia*-ESO benchmark star and we revised its stellar parameters here. A further five stars have also been proposed as possible benchmark stars by Heiter et al. (2015).

We determined angular diameters for the targets using data from the PAVO beam combiner at the CHARA Array. For three of the stars, we present new observations. For the other four stars, we reanalysed previous observations to ensure the stellar parameters were determined consistently. Limb-darkening coefficients

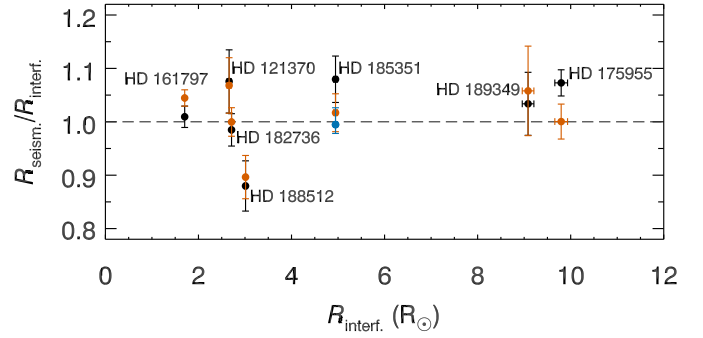


Fig. 8. Comparison of radii determined from asteroseismic scaling relations (uncorrected in black, corrected in orange) and modelling (blue) with interferometric radii from this work.

were determined from the STAGGER grid of 3D hydrodynamic stellar model atmospheres.

We computed bolometric fluxes from multi-band photometry, interpolating iteratively on a grid of synthetic stellar fluxes to ensure consistency with the final adopted stellar parameters. Effective temperatures were determined directly from the angular diameters and bolometric fluxes.

We determined $[\text{Fe}/\text{H}]$ based on high-resolution spectroscopy. We used isochrone fitting to derive mass, and parallax measurements to constrain the absolute luminosity. After iterative refinement between interferometry, spectroscopy and photometry we derived the final fundamental parameters of T_{eff} , $\log g$, and $[\text{Fe}/\text{H}]$ for all stars.

For six of our seven targets, we reached the desired precision of $\approx 1\%$ in T_{eff} . Only one star (HD 189349) showed a somewhat larger T_{eff} uncertainty of 2%. The T_{eff} uncertainty for this star is dominated by uncertainty in the bolometric flux. We do not recommend that this star be used as a benchmark until its bolometric flux can be more reliably measured. For the surface gravity, $\log g$, we reached a median precision of 0.034 dex and for metallicity $[\text{Fe}/\text{H}]$, we reached a median precision of 0.07 dex.

The giant and subgiant stars presented here, in conjunction with our previous results for metal-poor (Karovicova et al. 2020) and dwarf stars (Karovicova et al. 2021), form a sample of benchmark stars with consistently derived, highly reliable fundamental stellar parameters. The precision we have been able to achieve is essential to a consistent and reliable calibration of atmospheric parameters across large spectroscopic surveys. Consequently, the correctly determined atmospheric parameters will help us to better understand the evolution of stars in the Milky Way.

Acknowledgements. I.K. acknowledges the German Deutsche Forschungsgemeinschaft, DFG project number KA4055 and the European Science Foundation – GREAT *Gaia* Research for European Astronomy Training. This work is based upon observations obtained with the Georgia State University Center for High Angular Resolution Astronomy Array at Mount Wilson Observatory. The CHARA Array is supported by the National Science Foundation under Grants No. AST-1211929 and AST-1411654. Institutional support has been provided from the GSU College of Arts and Sciences and the GSU Office of the Vice President for Research and Economic Development. Funding for the Stellar Astrophysics Centre is provided by The Danish National Research Foundation. L.C. is the recipient of the ARC Future Fellowship FT160100402. T.N. acknowledges funding from the Australian Research Council (grant DP150100250). Parts of this research were conducted by the Australian Research Council Centre of Excellence for All Sky Astrophysics in 3 Dimensions (ASTRO 3D), through project number CE170100013. D.H. acknowledges support from the Alfred P. Sloan Foundation, the National Aeronautics and Space Administration (80NSSC19K0379), and the National Science Foundation (AST-1717000).

This work is based on spectral data retrieved from the ELODIE archive at Observatoire de Haute-Provence (OHP).

References

- Allende Prieto, C., Majewski, S. R., Schiavon, R., et al. 2008, *Astron. Nachr.*, **329**, 1018
- Amarsi, A. M., Lind, K., Asplund, M., Barklem, P. S., & Collet, R. 2016, *MNRAS*, **463**, 1518
- Baines, E. K., Armstrong, J. T., Schmitt, H. R., et al. 2014, *ApJ*, **781**, 90
- Baines, E. K., Armstrong, J. T., Schmitt, H. R., et al. 2018, *AJ*, **155**, 30
- Barklem, P. S., & Asplund-Johansson, J. 2005, *A&A*, **435**, 373
- Barklem, P. S., Piskunov, N., & O'Mara, B. J. 2000, *A&AS*, **142**, 467
- Bazot, M., Ireland, M. J., Huber, D., et al. 2011, *A&A*, **526**, L4
- Belokurov, V., Penoyre, Z., Oh, S., et al. 2020, *MNRAS*, **496**, 1922
- Bessell, M. S. 2000, *PASP*, **112**, 961
- Bonanno, A., Benatti, S., Claudi, R., et al. 2008, *ApJ*, **676**, 1248
- Boyajian, T. S., McAlister, H. A., van Belle, G., et al. 2012a, *ApJ*, **746**, 101
- Boyajian, T. S., von Braun, K., van Belle, G., et al. 2012b, *ApJ*, **757**, 112
- Boyajian, T. S., von Braun, K., van Belle, G., et al. 2013, *ApJ*, **771**, 40
- Boyajian, T. S., van Belle, G., & von Braun, K. 2014, *AJ*, **147**, 47
- Broggaard, K., Hansen, C. J., Miglio, A., et al. 2018, *MNRAS*, **476**, 3729
- Brown, T. M., Gilliland, R. L., Noyes, R. W., & Ramsey, L. W. 1991, *ApJ*, **368**, 599
- Carrier, F., Eggenberger, P., & Bouchy, F. 2005, *A&A*, **434**, 1085
- Casagrande, L., & Vandenberg, D. A. 2014, *MNRAS*, **444**, 392
- Casagrande, L., & Vandenberg, D. A. 2018, *MNRAS*, **475**, 5023
- Christensen-Dalsgaard, J., Bedding, T. R., & Kjeldsen, H. 1995, *ApJ*, **443**, L29
- Claret, A. 2000, *A&A*, **363**, 1081
- Claret, A., & Bloemen, S. 2011, *A&A*, **529**, A75
- Corsaro, E., Grundahl, F., Leccia, S., et al. 2012, *A&A*, **537**, A9
- de Jong, R. S., Bellido-Tirado, O., Chiappini, C., et al. 2012, in *Ground-based and Airborne Instrumentation for Astronomy IV*, eds. I. S. McLean, S. K. Ramsay, & H. Takami, *SPIE Conf. Ser.*, **8446**, 84460T
- De Silva, G. M., Freeman, K. C., Bland-Hawthorn, J., et al. 2015, *MNRAS*, **449**, 2604
- Derekas, A., Kiss, L. L., Borkovits, T., et al. 2011, *Science*, **332**, 216
- Di Mauro, M. P., Christensen-Dalsgaard, J., Kjeldsen, H., Bedding, T. R., & Paternò, L. 2003, *A&A*, **404**, 341
- Dotter, A., Chaboyer, B., Jevremović, D., et al. 2008, *ApJS*, **178**, 89
- ESA. 1997, *ESA, 1997, The Hipparcos and Tycho catalogues*, ESA SP, 1200
- Evans, D. W., Riello, M., De Angeli, F., et al. 2018, *A&A*, **616**, A4
- Gaia Collaboration (Prusti, T., et al.) 2016, *A&A*, **595**, A1
- Gilmore, G., Randich, S., Asplund, M., et al. 2012, *The Messenger*, **147**, 25
- Green, G. M., Schlafly, E. F., Finkbeiner, D. P., et al. 2015, *ApJ*, **810**, 25
- Grundahl, F., Fredslund Andersen, M., Christensen-Dalsgaard, J., et al. 2017, *ApJ*, **836**, 142
- Guggenberger, E., Hekker, S., Basu, S., & Bellinger, E. 2016, *MNRAS*, **460**, 4277
- Gustafsson, B., Edvardsson, B., Eriksson, K., et al. 2008, *A&A*, **486**, 951
- Heiter, U., Jofré, P., Gustafsson, B., et al. 2015, *A&A*, **582**, A49
- Hjørringgaard, J. G., Silva Aguirre, V., White, T. R., et al. 2017, *MNRAS*, **464**, 3713
- Høg, E., Fabricius, C., Makarov, V. V., et al. 2000, *A&A*, **355**, L27
- Huber, D., Ireland, M. J., Bedding, T. R., et al. 2012, *ApJ*, **760**, 32
- Huber, D., Zinn, J., Bojsen-Hansen, M., et al. 2017, *ApJ*, **844**, 102
- Ireland, M. J., Mérand, A., ten Brummelaar, T. A., et al. 2008, in *Optical and Infrared Interferometry*, Proc. SPIE, 7013, 701324
- Jofré, P., Heiter, U., Soubiran, C., et al. 2014, *A&A*, **564**, A133
- Jofré, P., Heiter, U., Soubiran, C., et al. 2015, *A&A*, **582**, A81
- Johnson, J. A., Huber, D., Boyajian, T., et al. 2014, *ApJ*, **794**, 15
- Joyce, M., & Chaboyer, B. 2018, *ApJ*, **864**, 99
- Kallinger, T., Weiss, W. W., Barban, C., et al. 2010, *A&A*, **509**, A77
- Karovicova, I., White, T. R., Nordlander, T., et al. 2018, *MNRAS*, **475**, L81
- Karovicova, I., White, T. R., Nordlander, T., et al. 2020, *A&A*, **640**, A25
- Karovicova, I., White, T. R., Nordlander, T., et al. 2021, *A&A*, **658**, A47
- Kervella, P., Arenou, F., Mignard, F., & Thévenin, F. 2019, *A&A*, **623**, A72
- Kjeldsen, H., & Bedding, T. R. 1995, *A&A*, **293**, 87
- Kjeldsen, H., Bedding, T. R., Baldry, I. K., et al. 2003, *AJ*, **126**, 1483
- Lebzelter, T., Heiter, U., Abia, C., et al. 2012, *A&A*, **547**, A108
- Li, T., Bedding, T. R., Kjeldsen, H., et al. 2019, *MNRAS*, **483**, 780
- Ligi, R., Creevey, O., Mourard, D., et al. 2016, *A&A*, **586**, A94
- Lin, J., Dotter, A., Ting, Y.-S., & Asplund, M. 2018, *MNRAS*, **477**, 2966
- Maestro, V., Che, X., Huber, D., et al. 2013, *MNRAS*, **434**, 1321
- Magic, Z., Collet, R., Asplund, M., et al. 2013, *A&A*, **557**, A26
- Magic, Z., Chiavassa, A., Collet, R., & Asplund, M. 2015, *A&A*, **573**, A90
- Mason, B. D., Wycoff, G. L., Hartkopf, W. I., Douglass, G. G., & Worley, C. E. 2001, *AJ*, **122**, 3466
- Moultaka, J., Ilovaisky, S. A., Prugniel, P., & Soubiran, C. 2004, *PASP*, **116**, 693
- Mozurkewich, D., Armstrong, J. T., Hindsley, R. B., et al. 2003, *AJ*, **126**, 2502
- Nordgren, T. E., Germain, M. E., Benson, J. A., et al. 1999, *AJ*, **118**, 3032
- Nordgren, T. E., Sudol, J. J., & Mozurkewich, D. 2001, *AJ*, **122**, 2707
- O'Donnell, J. E. 1994, *ApJ*, **422**, 158
- Piskunov, N., & Valenti, J. A. 2017, *A&A*, **597**, A16
- Quirrenbach, A., Mozurkewich, D., Buscher, D. F., Hummel, C. A., & Armstrong, J. T. 1996, *A&A*, **312**, 160
- Rabus, M., Lachaume, R., Jordán, A., et al. 2019, *MNRAS*, **484**, 2674
- Rains, A. D., Ireland, M. J., White, T. R., Casagrande, L., & Karovicova, I. 2020, *MNRAS*, **493**, 2377
- Rains, A. D., Žerjal, M., Ireland, M. J., et al. 2021, *MNRAS*, **504**, 5788
- Randich, S., Gilmore, G., & Gaia-ESO Consortium. 2013, *The Messenger*, **154**, 47
- Roberts, L. C. J., Mason, B. D., Aguilar, J., et al. 2016, *AJ*, **151**, 169
- Rodrigues, T. S., Bossini, D., Miglio, A., et al. 2017, *MNRAS*, **467**, 1433
- Sahlholdt, C. L., Feltzing, S., Lindegren, L., & Church, R. P. 2019, *MNRAS*, **482**, 895
- Sharma, S., Stello, D., Bland-Hawthorn, J., Huber, D., & Bedding, T. R. 2016, *ApJ*, **822**, 15
- Skrutskie, M. F., Cutri, R. M., Stiening, R., et al. 2006, *AJ*, **131**, 1163
- Straka, C. W., Demarque, P., Guenther, D. B., Li, L., & Robinson, F. J. 2006, *ApJ*, **636**, 1078
- Takeda, Y., & Tajitsu, A. 2015, *MNRAS*, **450**, 397
- Tayar, J., Claytor, Z. R., Huber, D., & van Saders, J. 2020, ArXiv e-prints [arXiv:2012.07957]
- Telting, J. H., Avila, G., Buchhave, L., et al. 2014, *Astron. Nachr.*, **335**, 41
- Ten Brummelaar, T. A., McAlister, H. A., Ridgway, S. T., et al. 2005, *ApJ*, **628**, 453
- Thévenin, F., Kervella, P., Pichon, B., et al. 2005, *A&A*, **436**, 253
- Ulrich, R. K. 1986, *ApJ*, **306**, L37
- van Belle, G. T., Ciardi, D. R., & Boden, A. F. 2007, *ApJ*, **657**, 1058
- Viani, L. S., Basu, S., Chaplin, W. J., Davies, G. R., & Elsworth, Y. 2017, *ApJ*, **843**, 11
- von Braun, K., Boyajian, T. S., van Belle, G. T., et al. 2014, *MNRAS*, **438**, 2413
- White, T. R., Bedding, T. R., Stello, D., et al. 2011, *ApJ*, **743**, 161
- White, T. R., Huber, D., Maestro, V., et al. 2013, *MNRAS*, **433**, 1262
- White, T. R., Huber, D., Mann, A. W., et al. 2018, *MNRAS*, **477**, 4403
- Yu, J., Huber, D., Bedding, T. R., et al. 2018, *ApJS*, **236**, 42

Appendix A: Limb-darkening coefficients in 38 channels.**Table A.1.** Limb-darkening coefficients in 38 channels. We show one table for the star HD 121370 as an example. Limb-darkening coefficients for the rest of the stars are available at CDS in tables A.1.–A.7.

HD 121370					
four-term limb-darkening ^a					
chan.	wavelength	a_1	a_2	a_3	a_4
1.	0.630	1.967	-3.239	3.420	-1.258
2.	0.635	1.967	-3.242	3.418	-1.256
3.	0.639	1.975	-3.255	3.422	-1.256
4.	0.644	1.995	-3.317	3.496	-1.290
5.	0.649	2.004	-3.340	3.507	-1.290
6.	0.654	2.066	-3.434	3.546	-1.311
7.	0.659	2.068	-3.448	3.556	-1.311
8.	0.664	1.989	-3.302	3.458	-1.276
9.	0.670	1.996	-3.329	3.485	-1.283
10.	0.675	1.993	-3.323	3.470	-1.276
11.	0.680	1.997	-3.335	3.477	-1.277
12.	0.686	2.004	-3.359	3.501	-1.286
13.	0.692	2.006	-3.362	3.495	-1.282
14.	0.698	2.015	-3.394	3.529	-1.296
15.	0.704	2.021	-3.417	3.552	-1.305
16.	0.710	2.024	-3.426	3.556	-1.307
17.	0.716	2.040	-3.473	3.604	-1.325
18.	0.722	2.039	-3.476	3.604	-1.325
19.	0.729	2.038	-3.475	3.592	-1.316
20.	0.736	2.041	-3.488	3.606	-1.323
21.	0.743	2.055	-3.534	3.649	-1.337
22.	0.750	2.049	-3.517	3.627	-1.330
23.	0.756	2.045	-3.510	3.618	-1.327
24.	0.763	2.054	-3.539	3.643	-1.336
25.	0.771	2.051	-3.537	3.639	-1.334
26.	0.778	2.058	-3.563	3.670	-1.349
27.	0.786	2.047	-3.533	3.626	-1.329
28.	0.794	2.058	-3.569	3.663	-1.343
29.	0.802	2.055	-3.569	3.661	-1.342
30.	0.810	2.053	-3.568	3.658	-1.342
31.	0.818	2.062	-3.600	3.687	-1.352
32.	0.827	2.053	-3.578	3.661	-1.341
33.	0.835	2.065	-3.617	3.700	-1.356
34.	0.844	2.055	-3.592	3.669	-1.344
35.	0.853	2.065	-3.620	3.687	-1.347
36.	0.863	2.058	-3.609	3.673	-1.341
37.	0.872	2.067	-3.646	3.715	-1.361
38.	0.881	2.060	-3.633	3.708	-1.363

Notes. ^a Limb-darkening coefficients derived from the grid of [Magic et al. \(2015\)](#); see text for details.